PHYSICAL REVIEW E **98**, 013306 (2018)

Three-dimensional multidomain lattice Boltzmann grid refinement for passive scalar transport

Tong-Miin Liou[*] and Chun-Sheng Wang
Department of Power Mechanical Engineering, National Tsing Hua University, Hsinchu 30013, Taiwan

(Received 11 November 2017; revised manuscript received 3 April 2018; published 24 July 2018)

Simulations of passive scalar transport on a three-dimensional (3D) multiresolution grid are presented within the framework of single relaxation time lattice Boltzmann method. The combined modeling of the fluid flow and scalar transport is handled by a double distribution function approach in which the velocity in the fluid flow equation is solved first and then copied to the scalar equation to solve the corresponding scalar quantities. A 3D scaling technique, considering both external forces and scalar source terms, and two-dimensional bicubic interpolation scheme are developed for coupling nonequilibrium velocity and scalar distributions on the interfaces of different resolution grids. The proposed algorithm is validated for three benchmark cases, i.e., the forced convection in a 3D channel, natural convection in a cubical cavity, and turbulent channel flow with heat transfer. Good agreements are found between the present predictions and previous data, which confirms the capability of the proposed method for the computation of passive scalar transport in 3D domains.

DOI: 10.1103/PhysRevE.98.013306

I. INTRODUCTION

The lattice Boltzmann method (LBM) has emerged as an efficient numerical tool for computing fluid flows problems in recent two decades. Due to its origin from the lattice gas automata, LBM generally solves the lattice Boltzmann equation (LBE) in a uniform-sized mesh. Consequently, to obtain accurate results, the mesh size has to be adjusted to resolve the smallest scales, which means a surge in computational cost, especially for flows with high Reynold numbers. Nonetheless, appropriate techniques can be implemented to locally refine the mesh where the smallest scales are located, thus reducing the requirement of computational power without losing the accuracy. These approaches are called the multidomain LBM or multiresolution LBM. Unlike the conventional methods based on Navier-Stokes equations, there is a lack of sufficient research involving grid refinement algorithms in the framework of LBM.

Specifically, Filippova and Hänel [1] first proposed the method of two-dimensional (2D) grid refinement within the single-relaxation-time (SRT) LBM. A refinement scheme based on the scaling post-collision distribution functions is formulated based on the Chapman-Enskog expansion. The scheme was validated by simulating a benchmark problem of athermal flow around a 2D cylinder. They showed that the method is reliable, accurate, and efficient for simulating laminar incompressible flows. Dupuis and Chopard [2] further developed a 2D post-streaming distribution function scaling approach without singularity of relaxation time for SRT-LBM. It was claimed that the scheme is accurate and has no limitation of the relaxation time and overcomes some drawbacks of the existing approaches [1]. A Poiseuille flow is further simulated to test the algorithm and a speedup ratio of 1000 is found by using a hierarchy grid. Chen *et al.* [3] introduced a volumetric formulation of 2D grid refinement in which conservation laws at the boundaries of different level grids are exactly satisfied for SRT-LBM. The fluid flow past a 2D cylinder was chosen to validate interface updating technique. It was concluded that the conserving boundary schemes are very robust for the simulation of highly oscillating fluid flows. Rohde *et al.* [4] developed a three-dimensional (3D) mass conservative method without rescaling or interpolation of the distribution function for SRT-LBM. The selected benchmarks are Poiseuille flow, lid-driven cavity flow, and turbulent channel flow. They concluded that the good agreements for both laminar flow and turbulent first and second order statistics show the capability of the proposed approach for complex flows. Freitas *et al.* [5] further explored the refinement method of Filippova and Hänel [1] to simulate Poiseuille, cavity, and 3D turbulent channel flows. They come up with an algorithm in which the transformation and interpolation operations are formulated independent of the applied LBM scheme and allow the application of arbitrary collision models. Lagrava *et al.* [6] proved that the direct copy of distribution functions causes numerical instability at relatively high Reynolds number within the 2D rescaling and interpolation grid refinement algorithm. A nonweighted filtering technique of the nonequilibrium part of distribution functions is proposed and validated for flow past a cylinder and 2D dipole collision. Touil *et al.* [7] addressed the LBM based large eddy simulation (LES) in a 3D multidomain grid. A rescaling method based on the subscale grid viscosity was introduced. It was claimed that the approach demonstrates comparable results with those of the direct numerical simulation (DNS). Guzik *et al.* [8] studied the influence of interpolation methods on the accuracy of multidomain LBM. A spatial and temporal interpolation and mass conservative scheme was formulated. By simulating the transient Poiseuille flow, 2D and 3D Taylor–Green vortex, and flow around a 2D cylinder, it was found that the interpolation scheme is basically of second-order accuracy. Fakhari *et al.* [9] compared the standard LBM with the finite-difference based LBM (FDLBM) on 3D multidomain grids. They concluded that the standard LBM is more efficient than the FDLBM

---

[*] tmliou@pme.nthu.edu.tw

whereas the latter demonstrated the advantage of stability at higher Reynolds numbers. Kuwata and Suga [10] proposed a mass and momentum imbalance-correction grid-refinement method to further improve the accuracy as well as the applicability of the multidomain grid refinement approach for SRT-LBM. It was claimed that the scheme can effectively minimize the unphysically discontinuous velocity distributions. Schoenherr *et al.* [11] implemented the nonequilibrium distribution rescaling refinement algorithm on multiresolution grids for both CPUs and GPUs. It was found that the multidomain grids produce almost no extra computational cost compared to that of the uniform counterparts since the temporal and spatial interpolation algorithms are both simple.

As far as the advection-diffusion equations or passive scalar are concerned, Alemani *et al.* [12] introduced two grid refinement techniques for reaction-diffusion problems within SRT-LBM. The first one relies on the matching of the interfacial concentration and fluxes, whereas the second one depends on the nested subgrids. It was found that the two methods show similarly good results. Stiebler *et al.* [13] further developed a multidomain scheme for advection-diffusion equations for SRT-LBM. Except for spatial and temporal interpolations, a scaling operation is introduced to guarantee the continuity of the macroscopic values at the multidomain interfaces. Huang *et al.* [14] explored a multidomain technique for the 2D passive scalar thermal LBM (TLBM) with a multiple-relaxation-time model. They showed that the proposed multidomain algorithm does not depreciate the convergence accuracy of LBM. Dorschner *et al.* [15] further extended the multidomain approach to entropic LBM (ELBM) and simulated incompressible, thermal, and compressible flows. It was found that the proposed multidomain LBM is very stable and allows for significant under-resolution while retaining accuracy. But that comes with more complex computation procedures and higher cost compared with SRT LBM

In summary, to the authors' knowledge, previous research of the multidomain LBM mainly focuses on flows without scalar transport or with only 2D scalar transport whereas the study of 3D scalar transport based multidomain LBM is limited. Since spatial interpolations, as well as external forces and scalar source terms in the 3D domain, may differ from those of the 2D domains, further validations of the multidomain LBM are required. Moreover, the transport of scalar quantities, such as temperature, concentration, and level set function, plays a pivotal role in tremendous realistic 3D engineering devices including heat exchangers, mixers, pollutant operators, etc., the development 3D of scalar transport with fluid flow in a multi-resolution grid is a necessity. In the present study, the 3D multidomain algorithm for scalar transport in a multiresolution grid will be proposed within the SRT lattice Boltzmann framework. The modeling of scalars and the fluid motion will be handled by a double distribution function (DDF) approach [16] due to feasibly adjustable Prandtl numbers. A scaling technique considering both external forces and scalar source terms will be proposed for coupling non-equilibrium velocity and scalar distribution functions on different resolution grids. Without generality, the temperature will be chosen as a passive scalar in the following simulation. The proposed algorithm is validated for three benchmark cases, i.e., the forced convection in a 3D channel, natural convection in a cubical cavity, and turbulent channel flow with heat transfer. The remaining sections are organized as follows. The DDF formulation of LBM with scalars and the fluid motion is reviewed in Sec. II. A coupling technique for scalar transport is introduced in Sec. III. Then in Sec. IV the numerical tests of 3D Poiseuille flow, cubical cavity flow, and turbulent channel flow are demonstrated. Finally, Sec. V summarizes the conclusions.

II. DOUBLE DISTRIBUTION FUNCTION LBM

The DDF SRT LBEs for fluid flow and for passive scalar heat transfer are given by

$$f_\alpha(\boldsymbol{x}+\boldsymbol{e}_\alpha\Delta t, t+\Delta t) = f_\alpha(\boldsymbol{x},t) - \frac{1}{\tau_\nu}\left[f_\alpha(\boldsymbol{x},t) - f_\alpha^{(\mathrm{eq})}(\boldsymbol{x},t)\right] + \Delta t\left(1-\frac{1}{2\tau_\nu}\right)F_\alpha, \tag{1}$$

$$g_\alpha(\boldsymbol{x}+e_\alpha\Delta t, t+\Delta t) = g_\alpha(\boldsymbol{x},t) - \frac{1}{\tau_g}\left[g_\alpha(\boldsymbol{x},t) - g_\alpha^{(\mathrm{eq})}(\boldsymbol{x},t)\right] + \Delta t S_\alpha, \tag{2}$$

where the distribution functions $f_\alpha(\boldsymbol{x},t)$ and $g_\alpha(\boldsymbol{x},t)$ represent the probability of locating a particle at position $\boldsymbol{x}$ and time t with velocity $\boldsymbol{e}_\alpha$. τ_ν and τ_g are nondimensional relaxation times for velocity and temperature, respectively.F_α and S_α are, respectively, the external force and energy source in the discrete lattice form. $\boldsymbol{e}_\alpha$ is the discrete velocity vector from Gauss–Hermite quadrature. In the present study, the D3Q19 and D3Q7 lattice models are employed for velocity and temperature simulation, respectively, as depicted in Fig. 1. The discrete velocity vectors and weighting factors for D3Q19 and D3Q7 lattice model read

$$\{\boldsymbol{e}_\alpha, w_\alpha\} = \begin{cases} c[(0,0,0)],\ 1/3 & \alpha = 0 \\ c[(\pm1,0,0),(0,\pm1,0),(0,0,\pm1)],\ 1/18 & \alpha = 1,2,\ldots,6 \\ c[(\pm1,\pm1,0),(\pm1,0,\pm1),(0,\pm1,\pm1)],\ 1/36 & \alpha = 7,8,\ldots,18 \end{cases} \tag{3}$$

and

$$\{\boldsymbol{e}_\alpha, w_\alpha\} = \begin{cases} c[(0,0,0)],\ 1/4 & \alpha = 0 \\ c[(\pm1,0,0),(0,\pm1,0),(0,0,\pm1)],\ 1/8 & \alpha = 1,2,\ldots.,6 \end{cases}, \tag{4}$$

respectively, where the lattice velocity c equals $\Delta x/\Delta t$. $f_\alpha^{(\mathrm{eq})}(\boldsymbol{x},t)$ and are $g_\alpha^{(\mathrm{eq})}(\boldsymbol{x},t)$ distribution functions at the equilibrium state. To reduce the compressible effect in LBM, the following equilibrium distribution function [17] for fluid

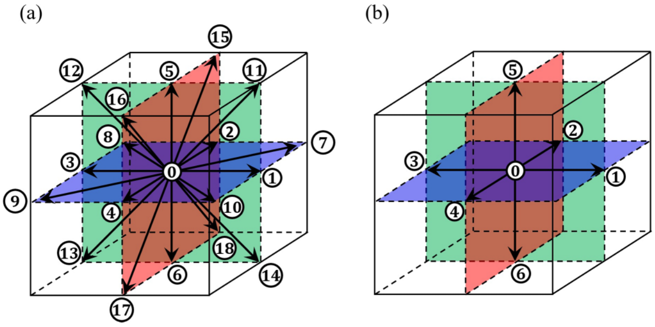

FIG. 1. (a) D3Q19 and (b) D3Q7 lattice models.

flow is considered:

$$f_\alpha^{(\mathrm{eq})}(\rho,\boldsymbol{u}) = w_\alpha\left[\rho + \rho_0\left(\frac{e_{\alpha i}u_i}{c_s^2} + \frac{Q_{\alpha ij}u_iu_j}{2c_s^4}\right)\right], \quad (5)$$

where ρ_0 is the reference density, $Q_{\alpha ij} = e_{\alpha i}e_{\alpha j} - c_s^2\delta_{ij}$, c_s and w_α are the dimensionless speed of sound and weighting factor, respectively; c_s is $c/\sqrt{3}$ for the D3Q19 lattice model. The equilibrium distribution function for heat transfer is expressed as

$$g_\alpha^{(\mathrm{eq})}(T,\boldsymbol{u}) = w_\alpha T\left[1 + \frac{e_{\alpha i}u_i}{c_s^2}\right], \quad (6)$$

where c_s equals $c/2$ for the D3Q7 lattice model. The external force term handled by the Guo's model [18] and the energy source term are given by

$$F_\alpha = w_\alpha\left[\frac{e_{\alpha i}F_i}{c_s^2} + \frac{(u_iF_j + F_iu_j)Q_{\alpha ij}}{2c_s^4}\right], \quad S_\alpha = w_\alpha S, \quad (7)$$

where F_i is the total macroscopic force and S_i is the energy source term. Then, the density, velocity, and temperature are determined by the moments of velocity and temperature distribution functions via

$$\rho = \sum_\alpha f_\alpha, \quad \rho_0\boldsymbol{u} = \sum_\alpha \boldsymbol{e}_\alpha f_\alpha + \frac{\Delta t}{2}\boldsymbol{F}, \quad T = \sum_\alpha g_\alpha. \quad (8)$$

By the Chapman-Enskog expansion of Eqs. (1) and (2), the corresponding incompressible Navier-Stokes equations are obtained as

$$\frac{\partial u_i}{\partial x_i} = 0, \quad (9)$$

$$\frac{\partial u_i}{\partial t} + \frac{\partial(u_ju_i)}{\partial x_j} = -\frac{1}{\rho_0}\frac{\partial p}{\partial x_i} + \frac{1}{\rho_0}F_i + \frac{\partial(2\nu S_{ij})}{\partial x_j}, \quad (10)$$

$$\frac{\partial T}{\partial t} + \frac{\partial(u_iT)}{\partial x_i} = \frac{\partial}{\partial x_j}\left(\alpha\frac{\partial T}{\partial x_j}\right) + S, \quad (11)$$

where the strain rate tensor S_{ij} is defined as $S_{ij} = 0.5(\partial u_i/\partial x_j + \partial u_j/\partial x_i)$. The kinematic viscosity ν and thermal diffusivity α are calculated from the relaxation times as

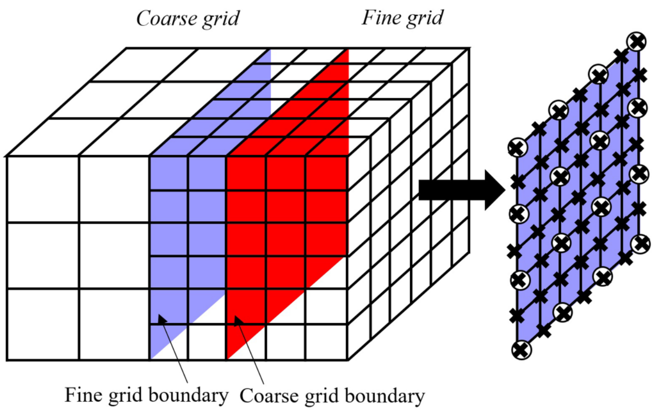

FIG. 2. Refinement boundaries between coarse and fine grids.

$$\nu = c_s^2\left(\tau_\nu - \tfrac{1}{2}\right)\Delta t, \quad \alpha = c_s^2\left(\tau_g - \tfrac{1}{2}\right)\Delta t, \quad (12)$$

respectively. Therefore, the Prandtl number Pr is defined by

$$\mathrm{Pr} = \frac{\nu}{\alpha} = \frac{4}{3}\frac{2\tau_\nu - 1}{2\tau_g - 1}. \quad (13)$$

Another important aspect of DDF-LBM is about the boundary conditions. In this study, the boundary treatment technique of Malaspinas and Sagaut [19,20] will be employed. It is based on the Zou and He hypothesis [21] but reconstructs the non-equilibrium distribution function from the non-equilibrium stress tensor. The method shows advantages of both accuracy and stability.

III. 3D MULTIDOMAIN LBM WITH SCALAR TRANSPORT

The 3D multidomain grids with two-level refinement are shown in Fig. 2. For brevity's sake, let subscript c denote the coarse grids and f denote the fine grids. There exist two kinds of scaling strategies between space and time, that is the convective scaling and the diffusive scaling. Here the convective scaling is adopted [6], where the spatial and temporal resolutions between coarse and fine grids are given as $\Delta x_f/\Delta x_c = \Delta t_f/\Delta t_c = n$. Here n is the grid refinement ratio. To exchange information between the fine grid boundary (2D plane marked with blue color in Fig. 2) and the coarse grid boundary (2D plane marked with red color in Fig. 2), the width of the overlapping zone is set to one coarse grid.

According to the Chapman-Enskog expansion, the distribution functions can be decomposed as series of a small parameter ε whose order of magnitude equals the Knudsen number, i.e.,

$$f_\alpha = f_\alpha^{(0)} + \varepsilon f_\alpha^{(1)} + \varepsilon^2 f_\alpha^{(2)} + \cdots, \quad (14)$$

$$\frac{\partial}{\partial t} = \varepsilon\frac{\partial}{\partial t_1} + \varepsilon^2\frac{\partial}{\partial t_2}, \quad \frac{\partial}{\partial x_i} = \varepsilon\frac{\partial}{\partial x_{i1}}, \quad (15)$$

and

$$\boldsymbol{F} = \varepsilon\boldsymbol{F}^{(1)}. \quad (16)$$

Then, by the Taylor expansion, Eq. (1) can be rewritten as

$$\Delta t\left(\frac{\partial}{\partial t}+e_{\alpha i}\frac{\partial}{\partial x_i}\right)f_\alpha+\frac{1}{2}\Delta t^2\left(\frac{\partial}{\partial t}+e_{\alpha i}\frac{\partial}{\partial x_i}\right)^2 f_\alpha+O(\Delta t^3)$$
$$=-\frac{1}{\tau_\nu}\left[f_\alpha-f_\alpha^{(\mathrm{eq})}\right]+\Delta t\left(1-\frac{1}{2\tau_\nu}\right)F_\alpha. \tag{17}$$

Substituting Eqs. (14)–(16) into Eq. (17) and rewriting them in the consecutive orders of ε as

$$\varepsilon^0 : f_\alpha^{(0)}=f_\alpha^{(\mathrm{eq})}, \tag{18}$$

$$\varepsilon^1 : \left(\frac{\partial}{\partial t_1}+e_{\alpha i}\frac{\partial}{\partial x_{i1}}\right)f_\alpha^{(0)}-F_\alpha^{(1)}$$
$$=-\frac{1}{\Delta t\tau_\nu}\left[f_\alpha^{(1)}+\frac{\Delta t}{2}F_\alpha^{(1)}\right], \tag{19}$$

$$\varepsilon^2 : \frac{\partial f_\alpha^{(0)}}{\partial t_2}+\left(1-\frac{1}{2\tau_\nu}\right)\left(\frac{\partial}{\partial t_1}+e_{\alpha i}\frac{\partial}{\partial x_{i1}}\right)\left[f_\alpha^{(1)}+\frac{\Delta t}{2}F_\alpha^{(1)}\right]$$
$$=-\frac{1}{\Delta t\tau_\nu}f_\alpha^{(2)}. \tag{20}$$

Note that the macroscopic quantities, including density, velocity, external force, temperature, and energy source, remain invariant to the grid resolution, i.e., $\rho_c=\rho_f$, $\boldsymbol{u}_c=\boldsymbol{u}_f$, $T_c=T_f$, $\boldsymbol{F}_c=\boldsymbol{F}_f$, and $S_c=S_f$. The equilibrium distribution functions, external force, and energy source in momentum space, which are composite functions of macroscopic quantities, are therefore also independent of grid resolutions, namely $f_{\alpha,c}^{(\mathrm{eq})}=f_{\alpha,f}^{(\mathrm{eq})}$, $g_{\alpha,c}^{(\mathrm{eq})}=g_{\alpha,f}^{(\mathrm{eq})}$, $F_{\alpha,c}=F_{\alpha,f}$, and $S_{\alpha,c}=S_{\alpha,f}$. The right-hand side of Eq. (19) can be expressed as

$$\frac{1}{\Delta t_c\tau_{\nu,c}}\left[f_{\alpha,c}^{(1)}+\frac{\Delta t_c}{2}F_{\alpha,c}^{(1)}\right]=\frac{1}{\Delta t_f\tau_{\nu,f}}\left[f_{\alpha,f}^{(1)}+\frac{\Delta t_f}{2}F_{\alpha,f}^{(1)}\right]. \tag{21}$$

Since the nonequilibrium part $f_\alpha^{(\mathrm{neq})}=f_\alpha-f_\alpha^{(\mathrm{eq})}\approx\varepsilon f_\alpha^{(1)}$, Eq. (21) is further rearranged as

$$\frac{1}{\Delta t_c\tau_{\nu,c}}\left[f_{\alpha,c}^{(\mathrm{neq})}+\frac{\Delta t_c}{2}F_{\alpha,c}\right]=\frac{1}{\Delta t_f\tau_{\nu,f}}\left[f_{\alpha,f}^{(\mathrm{neq})}+\frac{\Delta t_f}{2}F_{\alpha,f}\right]. \tag{22}$$

Similarly, by Chapman-Enskog and Taylor expansion, the following equations on temperature distribution functions are obtained

$$g_\alpha=g_\alpha^{(0)}+\varepsilon g_\alpha^{(1)}+\varepsilon^2 g_\alpha^{(2)}+\cdots, \tag{23}$$

$$S=\varepsilon S^{(1)}, \tag{24}$$

$$\Delta t\left(\frac{\partial}{\partial t}+e_{\alpha i}\frac{\partial}{\partial x_i}\right)g_\alpha+\frac{1}{2}\Delta t^2\left(\frac{\partial}{\partial t}+e_{\alpha i}\frac{\partial}{\partial x_i}\right)^2 g_\alpha+O(\Delta t^3)$$
$$=-\frac{1}{\tau_g}\left[g_\alpha-g_\alpha^{(\mathrm{eq})}\right]+\Delta t S_\alpha, \tag{25}$$

Combining Eqs. (15), (23), (24), and (25) and rearranging them in the consecutive orders of ε as

$$\varepsilon^0 : g_\alpha^{(0)}=g_\alpha^{(\mathrm{eq})}, \tag{26}$$

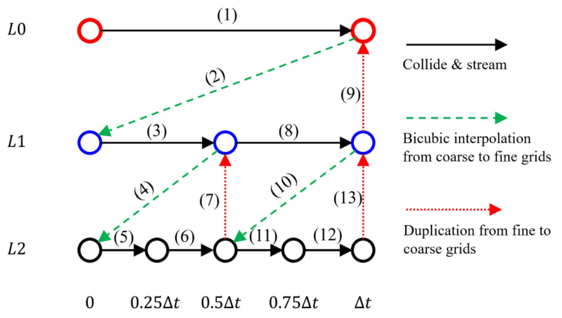

FIG. 3. Calculation processes for a three-level multidomain grid where the number in the bracket represents the order of operations.

$$\varepsilon^1 : \left(\frac{\partial}{\partial t_1}+e_{\alpha i}\frac{\partial}{\partial x_{i1}}\right)g_\alpha^{(0)}-S_{\alpha 1}=-\frac{1}{\Delta t\tau_g}g_\alpha^{(1)}, \tag{27}$$

$$\varepsilon^2 : \frac{\partial g_\alpha^{(0)}}{\partial t_2}+\left(1-\frac{1}{2\tau_g}\right)\left(\frac{\partial}{\partial t_1}+e_{\alpha i}\frac{\partial}{\partial x_{i1}}\right)g_\alpha^{(1)}$$
$$+\frac{\Delta t}{2}\left(\frac{\partial}{\partial t_1}+e_{\alpha i}\frac{\partial}{\partial x_{i1}}\right)S_{\alpha 1}=-\frac{1}{\Delta t\tau_g}g_\alpha^{(2)}, \tag{28}$$

Performing the aforementioned operations on Eq. (28), the scaling strategy for non-equilibrium scalar distribution function is given by

$$\frac{1}{\Delta t_c\tau_{g,c}}g_{\alpha,c}^{(\mathrm{neq})}=\frac{1}{\Delta t_f\tau_{g,f}}g_{\alpha,f}^{(\mathrm{neq})}. \tag{29}$$

Once the scaling strategy is established, a multidomain grid coupling of distribution functions can be carried out. Figure 3 shows the detailed streaming and collision process (black arrow), interpolation process (green arrow), and duplication process (red arrow) on a multidomain grid with three level resolutions (L0, L1, and L2). The order of operation in one cycle is indicated by the number in the bracket. The temporal interpolation scheme of the non-equilibrium distribution functions is linear whereas the spatial interpolation scheme is bicubic as shown in Fig. 4. A general expression of the third

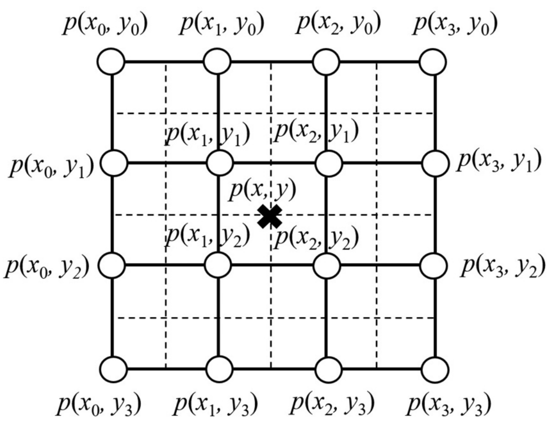

FIG. 4. Bicubic spatial interpolations from coarse to fine grids.

order bicubic interpolation is given by

$$p(x,y)=\sum_{i=0}^{3}\sum_{j=0}^{3}b_{ij}x^{i}y^{j}, \tag{30}$$

where the coefficients b_{ij} depends on the fine grid location. Specifically, for central nodes, a full 16-point bicubic interpolation scheme is used. For edge and corner nodes, a biased 12- and 9-point interpolation schemes are applied. A full 16-point bicubic interpolation scheme has also been tested for the Poiseuille flow case and found that biased interpolation does not affect the overall accuracy since the number of corner and edge nodes is marginal compared to overall grids. Therefore, to guarantee the parallel efficiency [6] (Only two envelope nodes are required for communication between different blocks), biased interpolations are adopted in the present study. Furthermore, the third-order bicubic interpolation is found to be mass conservative for a preliminary numerical test.

For copying distribution functions from fine to coarse grids, there exist two major filtering techniques, one is arithmetic average proposed by Lagrava *et al.* [6] and the other is weighted average proposed by Touil *et al.* [7]. The effect of filter has been tested in our cases. For laminar flow at relative low Reynolds number or Raleigh number, the filter is not necessary and does not affect the final results. However, for turbulent flow and cavity flow with higher Raleigh number, say 10^6 in our case, the adoption of filter can contribute to the stability of simulation with relatively coarse grids. In addition, there is no observable difference between arithmetic average and weighted average. Hence, in present study, a uniform filter is adopted.

IV. NUMERICAL RESULTS AND DISCUSSION

In this section, some benchmark cases will be simulated to validate the proposed 3D multidomain approach for passive scalar heat transfer. The first problem is the forced convection in a 3D channel with constant wall heat flux. This case involves both an external force in the fluid flow equation and a source term in the energy equation. The second problem is the natural convection in a cubical cavity. Unlike the first case, this case does not possess an energy source term, but its energy equations are coupled with the fluid flow equation through the Boussinesq approximation.

A. 3D Poiseuille flow with constant wall heat flux

A schematic diagram of pressure-driven Poiseuille flow in a 3D channel with heat transfer is depicted in Fig. 5. The streamwise (x), transverse (y), and spanwise (z) dimensions of the computational domain are set to $4h$, $2h$, and $2h$, respectively, where h is the half channel width fixed at 1. Periodic boundary conditions are assumed in x and z directions whereas in the transverse direction the top and bottom walls are assumed to be no-slip and with constant wall heat flux of q''. The flow is driven by a constant pressure gradient in the x-direction which is treated as an external body force term $F_1=\rho u_\tau^2/h$, where u_τ is the friction velocity. The periodic temperature boundary condition is realized by imposing a source term $S=q''/(\rho c_p h u_b)$ in the energy equation, where c_{p} is the specific heat and u_{b} is the bulk mean velocity. The analytical solutions for both velocity and temperature are expressed as

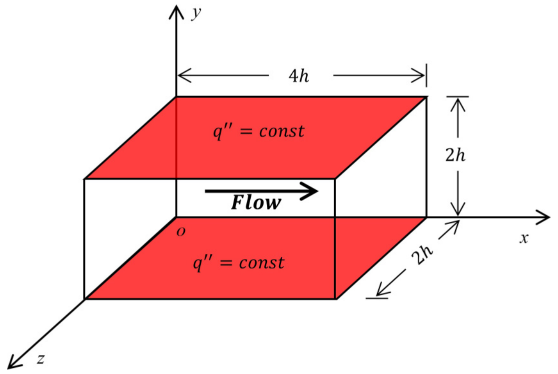

FIG. 5. Schematic diagram of the forced convection in a 3D channel.

$$u=\frac{1}{2}\mathrm{Re}_\tau u_\tau\left[2-\left(\frac{y}{h}\right)\right]\left(\frac{y}{h}\right), \tag{31}$$

$$\theta=-\frac{1}{8}\left[\left(\frac{y}{h}\right)-1\right]^4+\frac{3}{4}\left[\left(\frac{y}{h}\right)-1\right]^2+\theta_w-\frac{5}{8}, \tag{32}$$

where θ and θ_{w} is the dimensionless temperature and wall temperature normalized by $q''h/k$. The corresponding Nusselt number Nu, calculated by $4/(\theta_w-\theta_b)$, equals 8.235, where θ_{b} is the bulk mean temperature.

In the present study, the Reynolds number Re_τ, defined as $u_\tau h/\nu$, is fixed at 10. A working fluid air is employed, whose Pr equals 0.71. To test the multidomain algorithm, three grid systems named MG1, MG2, and MG3 are adopted as recorded in Table I. The grids are refined twice near the top and bottom walls as depicted in Fig. 6. The wall distances of the first and second refinement are $0.1h$ and $0.5h$, respectively. For the evaluation of Nusselt number, the trapezoid integration algorithm is adopted.

Figure 7 shows the transverse distributions of the streamwise velocities normalized by u_τ, u^+, and dimensionless temperature θ, obtained with the present multidomain LBM for the grid system of MG1. The blue and green arrows, denoted as L1-L0 and L2-L1, indicate the refinement locations between grid level 0 and level 1, and between grid level 1 and level 2, respectively. It is seen that the calculated velocity and temperature agree very well with the analytical solutions. Note that results of other two grid systems are not plotted here since they demonstrate no observable differences in u^+ and θ. As one further looks at the refinement interface L1-L0 and L2-L1, there exist no discontinuities of velocity or temperature. This

TABLE I. Grid configurations for the 3D channel flow ($h=1$).

Grid	Level 0 size	Level 1 size	Level 2 size
MG1	$h/8$	$h/16$	$h/32$
MG2	$h/10$	$h/20$	$h/40$
MG3	$h/16$	$h/32$	$h/64$

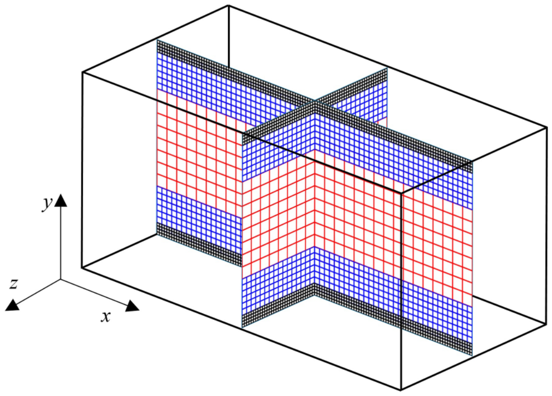

FIG. 6. Multidomain grid distributions on xy and yz midplanes of the channel.

is due to fact that the present method conserves the second order momentum and heat flux under the bicubic interpolation. In contrast, a grid system above $41 \times 41 \times 81$ is required to achieve the present accuracy on a uniform mesh.

To further test the accuracy of the method, Table II lists the simulated maximum and mean velocities, $u_{\max}$ and u_{b}, minimum and mean temperature, $\theta_{\min}$ and θ_{b}, and Nu compared with those of the analytical solution. The comparison shows a maximum relative error less than 1% for all grids and quantities examined. It is observed that the relative errors between calculated results and analytical solutions are decreasing with increasing number of grid points. The log error with respect to the log grid size gives a slope around 2 which further proves the second-order accuracy of the present method.

B. Natural convection in a cubical cavity

Since the channel flow problem does not consider the coupling between fluid flow equation and energy equation, another more complicated 3D benchmark case, i.e., the natural convection in a cubical cavity, will be simulated in this section. A sketch of the cubical cavity with natural convection is demonstrated in Fig. 8. Constant high and low temperature (T_{H} and T_{L}) boundary conditions are imposed on the right and left walls ($x = 0$ and $x = H$), respectively, whereas the remaining walls are maintained adiabatic. The flow is driven by a gravitational force $\boldsymbol{g}$, pointing towards the negative y-axis, as well as the corresponding buoyancy force. For moderate temperature difference, the flow inside the cavity is considered incompressible and the Boussinesq approximation is adopted to model the buoyancy force term, i.e., $\boldsymbol{F} = \rho_0 \boldsymbol{g} \beta (T - T_0)$, where β is the thermal expansion coefficient and T_0 is the reference temperature defined by $T_0 = (T_H + T_L)/2$. The Rayleigh number Ra and the characteristic velocity u_0 are defined by $\mathrm{Ra} = g\beta(T_H - T_L)H^3/(\alpha v)$ and $u_0 = \sqrt{g\beta(T_H - T_L)H}$, respectively. Similar to that of the channel flow, the air featuring a Prandtl number of 0.71 is chosen as working fluid. The overall Nusselt number Nu_{o} is determined by gradients of temperature on the heat walls as

$$\mathrm{Nu}_o = \int_0^H \int_0^H \left.\frac{\partial \theta}{\partial x}\right|_{x=0\ or\, H} dy\, dz, \tag{33}$$

where θ is the dimensionless temperature defined as $\theta = (T - T_L)/(T_H - T_L)$. In the present study, the Rayleigh number ranges from 10^3 to 10^6. To resolve the thermal boundary layer and the corner vortices, a three-level multidomain grid is generated as described in Fig. 9. The coarsest grids (level 0 grids) lie around the center of the domain with a fixed size of $H/32$ while the sizes of level 1 and level 2 grids are $H/64$ and $H/128$, respectively. The first and second refinement locations are $0.35H$ and $0.15H$ from the nearest walls.

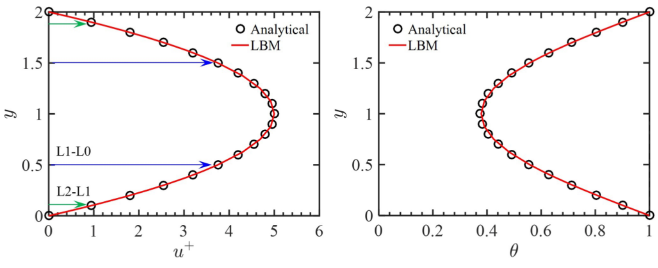

FIG. 7. Velocity and temperature profiles compared with the analytical results for the MG1 grid at $\mathrm{Re}_\tau = 10$ and $\mathrm{Pr} = 0.71$.

TABLE II. Comparisons of maximum and mean velocities, minimum and mean temperature, and Nusselt number with the analytical results at different grid resolutions for $\mathrm{Re}_\tau = 10$ and $\mathrm{Pr} = 0.71$.

Grid		$u_{\max}$	u_{b}	$\theta_{\min}$	θ_{b}	Nu
	Analytical	5	10/3	0.375	0.5143	8.235
MG1	Present	4.9986	3.3241	0.3786	0.5184	8.3058
	Error (%)	0.0283	0.2765	0.9485	0.7986	0.8594
MG2	Present	4.9992	3.3275	0.3771	0.5167	8.2769
	Error (%)	0.0164	0.1756	0.5499	0.4717	0.5085
MG3	Present	4.9998	3.3312	0.3756	0.5151	8.2496
	Error (%)	0.0035	0.0638	0.1645	0.1603	0.1765

Table III summarizes the present calculated results of maximum velocity components, $u_{\max}$ and $v_{\max}$, overall Nusselt numbers, Nu_{o}, and the corresponding coordinates compared with previous numerical data [22–24] on the $z = 0.5$ midplane. It is found that they are in reasonably good agreements with those from the literature for all Ra examined. The

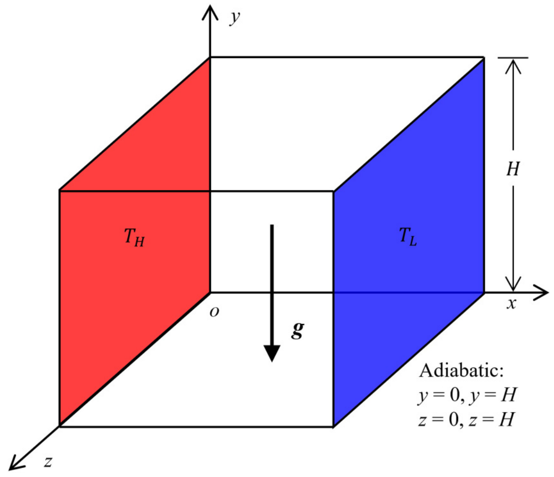

FIG. 8. Sketch of the natural convection in a cubical cavity.

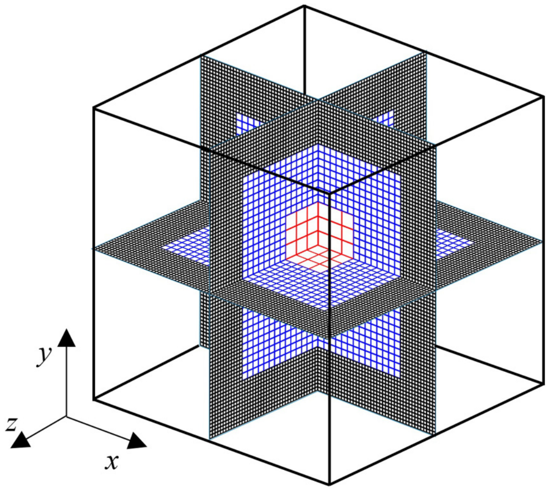

FIG. 9. Multidomain grid distributions on xy, xz, and yz midplanes of the cubical cavity.

negative discrepancies of Nu_o are due to weakly compressible characteristics of LBM, which can be further reduced by refining grid.

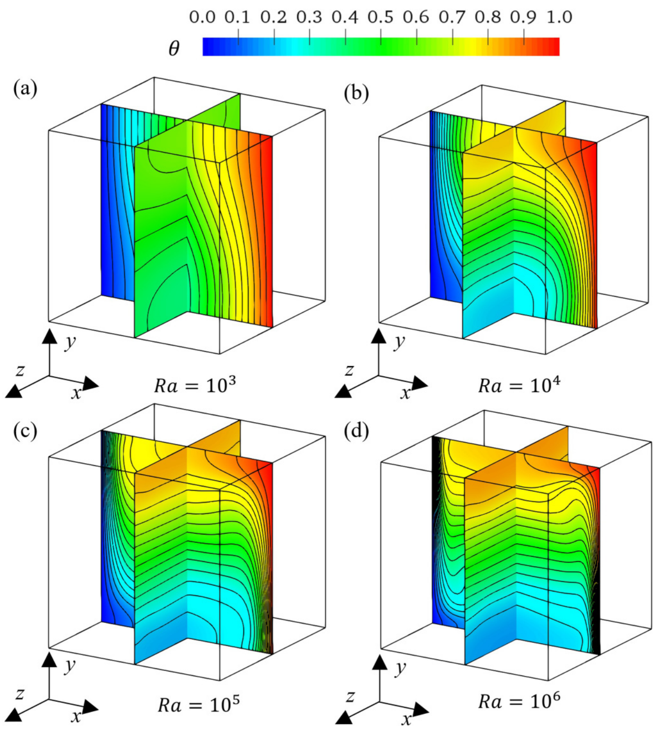

FIG. 10. Isotherms on $x = 0.5$ and $z = 0.5$ midplanes of the cubical cavity for (a) $\mathrm{Ra} = 10^3$, (b) $\mathrm{Ra} = 10^4$, (c) $\mathrm{Ra} = 10^5$, and (d) $\mathrm{Ra} = 10^6$.

Figures 10(a)–10(d) depict the isotherms on $x = 0.5$ and $z = 0.5$ planes for $\mathrm{Ra} = 10^3$, $\mathrm{Ra} = 10^4$, $\mathrm{Ra} = 10^5$, and $\mathrm{Ra} = 10^6$, respectively. Due to the existence of buoyancy forces, the temperature contours, indicated by the curved profiles of the isotherms, are not linearly distributed for all Ra examined. As the value of Ra increases from 10^3 to 10^6, the deviations from the vertically linear profile become more prominent, i.e., the nearly vertical isotherms turning horizontal (stratification) except the regions adjacent to the left and right walls. This is attributable to the enhanced effect of buoyancy which is implicitly proportional to the value of Ra. It is also observed that the temperature distributions at $x = 0.5$ plane are not uniform due to the influence of the side walls. Note that the above-mentioned temperature features at $z = 0.5$ are qualitatively similar to those of Wang *et al.* [24].

TABLE III. Maximum velocity components, overall Nusselt numbers, and the corresponding coordinates compared previous data [22–24] on $z = 0.5$ midplane for $\mathrm{Ra} = 10^3,\ 10^4,\ 10^5$, and 10^6.

Ra		$u_{\max}$	y	$v_{\max}$	x	Nu_o
10^3	Present	0.1331	0.1875	0.1332	0.8281	1.0673
	Ref. [22]	0.1314	0.2	0.132	0.8333	1.085
	Ref. [23]	0.132	0.188	0.133	0.826	1.075
	Ref. [24]	0.1315	0.1919	0.1326	0.8301	1.0700
10^4	Present	0.2007	0.1719	0.2235	0.8828	2.0468
	Ref. [22]	0.2013	0.1833	0.2252	0.8833	2.1
	Ref. [23]	0.206	0.163	0.221	0.887	2.085
	Ref. [24]	0.1968	0.1799	0.2218	0.8873	2.0535
10^5	Present	0.1457	0.1484	0.2479	0.9375	4.2936
	Ref. [22]	0.1468	0.1453	0.2471	0.9353	4.361
	Ref. [23]	0.149	0.136	0.240	0.935	4.378
	Ref. [24]	0.1426	0.1493	0.2442	0.9317	4.3248
10^6	Present	0.0819	0.1484	0.2616	0.9609	8.4909
	Ref. [22]	0.0841	0.1443	0.2588	0.9669	8.77
	Ref. [23]	–	–	–	–	–
	Ref. [24]	0.0816	0.1403	0.2556	0.9653	8.5428

The velocity magnitude, normalized by the characteristic velocity u_0, on $x = 0.5$ and $z = 0.5$ planes for $\mathrm{Ra} = 10^3$, $\mathrm{Ra} = 10^4$, $\mathrm{Ra} = 10^5$, and $\mathrm{Ra} = 10^6$, are plotted in Figs. 11(a)–11(d), respectively. It is noticeable that there exist four high-velocity regions near the four side walls indicating the existence of a large buoyancy induced a spherical vortex in the center of the cavity for $\mathrm{Ra} = 10^3$. The high-velocity fluid gradually concentrates around the left and right walls as Ra increases beyond 10^4 suggesting the vortex stretch. Since the increasing value of Ra leads to sharper temperature gradient near the left and right walls [Figs. 10(a)–10(d)], it results in greater buoyancy and, in turn, higher near-wall velocity.

C. 3D turbulent channel flow with heat transfer

To further validate the present multigrid model for turbulent flow and heat transfer, the 3D turbulent channel flow with heat transfer [25] is simulated in this section. Figure 12 depicts the schematic diagram of generic 3D turbulent channel flow. The streamwise, spanwise, and transverse dimension of computational domain are $2\pi\delta$, 2δ, and $\pi\delta$, respectively. The Reynolds number, based on the friction velocity u_τ and channel half height δ, i.e.,$\mathrm{Re}_\tau = u_\tau\delta/\nu$, is 180. A working fluid air is chosen, with Prandtl number $\mathrm{Pr} = 0.71$. The top and bottom walls are assumed to be no-slip and with constant higher (T_h) and lower temperature (T_c), respectively, and the rest of the walls are assumed to be periodic. The pressure gradient is treated as a body force $F = -dp/dx = \rho u_\tau^2/\delta$.

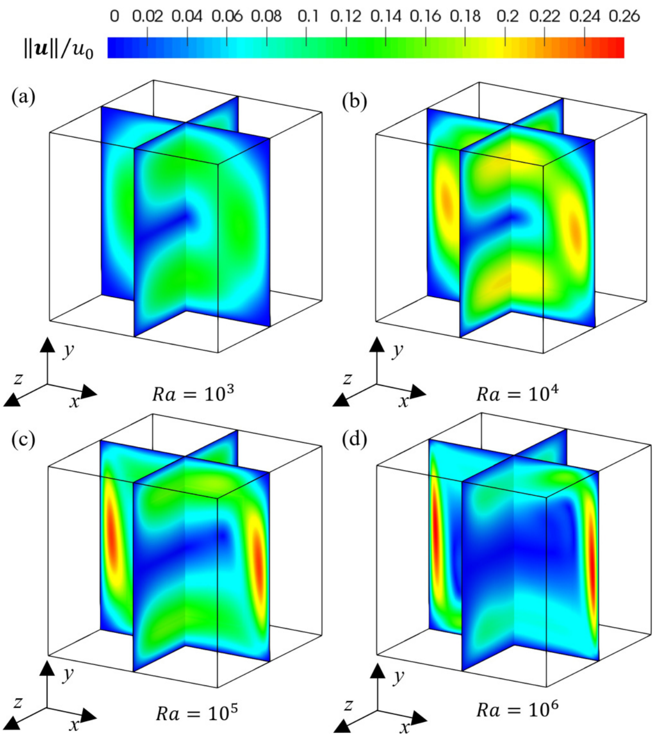

FIG. 11. Velocity magnitude normalized by the characteristic velocity $u_0 = \sqrt{g\beta(T_H - T_L)H}$ on $x = 0.5$ and $z = 0.5$ midplanes of the cubical cavity for (a) $\mathrm{Ra} = 10^3$, (b) $\mathrm{Ra} = 10^4$, (c) $\mathrm{Ra} = 10^5$, and (d) $\mathrm{Ra} = 10^6$.

To save the computational cost, the LES model with a Smagorinsky sub-grid closure and van Driest damping near the wall is used in this calculation. A two-level grid system, $280 \times 90 \times 140$ and $140 \times 45 \times 70$, is adopted, which corresponds to first layer $y+$ of 3.8. Similar to Fig. 6, the refinement distance is 0.4δ from the nearest wall. The initial velocity field is generated with one-seventh power law plus a random fluctuation within 5% of bulk mean velocity. The initial temperature field is specified with linear profile. The simulation is run for $100T^*$ until a statistical steady-state has been reached, where $T^* = \delta/u_\tau$ is turnover time. The turbulence statistics are collected from time-averaging over $20T^*$. The transverse profiles are calculated by averaging mean fields first along streamwise direction and then along spanwise direction.

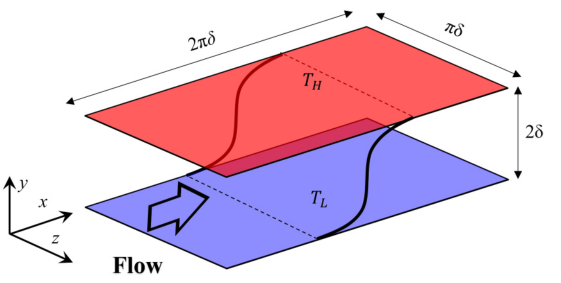

FIG. 12. Computational domain for 3D turbulent channel flow with heat transfer.

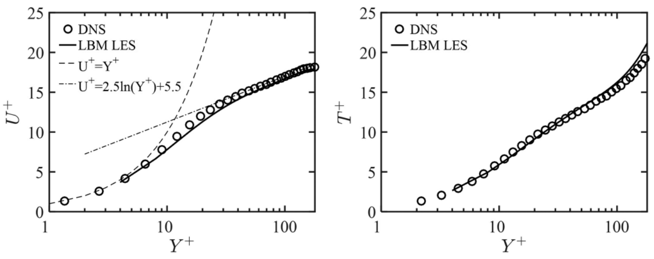

FIG. 13. Mean velocity and temperature profiles compared with DNS results [25].

Figure 13 shows streamwise mean velocity profile, $U^+ = U/U_\tau$, and mean temperature profile, $T^+ = (T - T_w)/T_\tau$, in near-wall coordinate, with $T_\tau = q_w/(\rho c_p u_\tau)$ and $q_w = -K(\partial T/\partial n)_w$. The law of wall and DNS data of Kawamura *et al.* [25] are also plotted for comparison. The calculated velocity shows reasonable agreement with log law results in viscous and log law region and a maximum difference around 3%, compared to that of DNS in the overlapping region, due to subgrid scale model in LES. It should be pointed out that the present data does not extend to $Y^+ = 1$ since the first layer grid distance is $Y^+ = 3.8$. Meanwhile, the temperature profile is also in good agreement with DNS data except a slight deviation in the core region. The overprediction is caused by the assumption of constant turbulent Prandtl number.

To examine the possible discontinuity of high order statistics as mentioned by Kuwata and Suga [10], Fig. 14 shows the $\langle u^+v^+\rangle$ Reynolds stress component and $\langle u^+\theta^+\rangle$ turbulent heat flux distributions along the y direction. For the Reynolds stress component, the linear profile of Reynolds stress, viscous stress, and total stress, i.e., $-\langle u^+v^+\rangle = 1 - Y^+/\mathrm{Re}_\tau - \partial U^+/\partial Y^+$, is plotted for further comparison. It is seen that the simulated result varies with Y^+ and agrees well with DNS results. Since the mean velocity gradient is close to zero around that area as depicted in Fig. 13, $\langle u^+v^+\rangle$ decreases linearly around horizontal midplane. In addition, the streamwise heat flux is also in a good match with DNS results with no discontinuity found in the grid refinement interface.

V. CONCLUSIONS

In the present study, the simulations of scalar transport on a 3D multidomain grid have been addressed within the LBM framework. A coupling technique and 2D interpolation method are proposed for scaling the velocity and passive scalar distribution functions in different resolution grids. The

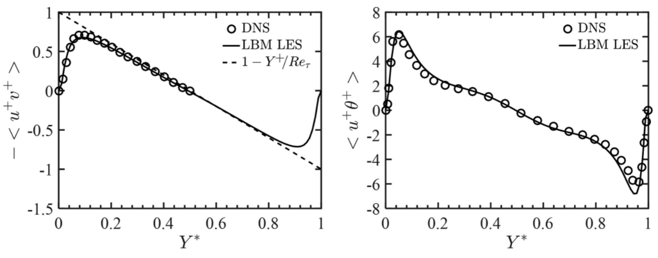

FIG. 14. Reynolds stress component and turbulent heat flux compared with DNS results [25].

proposed algorithm is validated for three benchmark cases, i.e., the forced convection in a 3D channel, natural convection in a cubical cavity, and turbulent channel flow with heat transfer. The good agreements with analytical solutions and previous benchmark data prove that the present approach can solve 3D scalar transport problems with both accuracy and efficiency. It should be pointed out that the present Rayleigh number or Reynold number is relatively small and does not cover a wider range of engineering applications. Therefore, the future work will be dedicated to applying the present multigrid LBM to the simulation of high Reynold number turbulent fluid flow with 3D passive scalar transport.

ACKNOWLEDGMENTS

The present research is sponsored by the Ministry of Science and Technology, Taiwan, under Contract No. MOST105-2221-E-007-058-MY3. The computer resources are provided by the Taiwan National Center for High-performance Computing.

---

[1] O. Filippova and D. Hänel, Grid refinement for lattice-BGK models, J. Comput. Phys. **147**, 219 (1998).

[2] A. Dupuis and B. Chopard, Theory and applications of an alternative lattice Boltzmann grid refinement algorithm, Phys. Rev. E **67**, 066707 (2003).

[3] H. Chen, O. Filippova, J. Hoch, K. Molvig, R. Shock, C. Teixeira, and R. Zhang, Grid refinement in lattice Boltzmann methods based on volumetric formulation, Physica A **362**, 158 (2006).

[4] M. Rohde, D. Kandhai, J. J. Derksen, and H. E. A. van den Akker, A Generic, mass conservative local grid refinement technique for lattice-Boltzmann schemes, Int. J. Numer. Methods Fluids **51**, 439 (2006).

[5] R. K. Freitas, M. Meinke, and W. Schröder, Turbulence simulation via the lattice-Boltzmann method on hierarchically refined meshes, in *Proceedings of the European Conference on Computational Fluid Dynamics* (TU Delft, The Netherlands, 2006), pp. 1–12.

[6] D. Lagrava, O. Malaspinas, J. Latt, and B. Chopard, Advances in multi-domain lattice Boltzmann grid refinement, J. Comput. Phys. **231**, 4808 (2012).

[7] H. Touil, D. Ricot, and E. Lévêque, Direct and large-eddy simulation of turbulent flows on composite multi-resolution grids by the lattice Boltzmann method, J. Comput. Phys. **256**, 220 (2014).

[8] S. M. Guzik, T. H. Weisgraber, P. Colella, and B. J. Alder, Interpolation methods and the accuracy of lattice-Boltzmann mesh refinement, J. Comput. Phys. **259**, 461 (2014).

[9] A. Fakhari and T. Lee, Numerics of the lattice Boltzmann method on nonuniform grids: Standard LBM and finite-difference LBM, Comput. Fluids **107**, 205 (2015).

[10] Y. Kuwata and K. Suga, Imbalance-correction grid-refinement method for lattice Boltzmann flow simulations, J. Comput. Phys. **311**, 348 (2016).

[11] M. Schönherr, K. Kucher, M. Geier, M. Stiebler, S. Freudiger, and M. Krafczyk, Multi-thread implementations of the lattice Boltzmann method on nonuniform grids for CPUs and GPUs, Comput. Math. Appl. **61**, 3730 (2011).

[12] D. Alemani, B. Chopard, J. Galceran, and J. Buffle, Two grid refinement methods in the lattice Boltzmann framework for reaction-diffusion processes in complex systems, Phys. Chem. Chem. Phys. **8**, 4119 (2006).

[13] M. Stiebler, J. Tölke, and M. Krafczyk, Advection-diffusion lattice Boltzmann scheme for hierarchical grids, Comput. Math. Appl. **55**, 1576 (2008).

[14] R. Huang and H. Wu, Multiblock approach for the passive scalar thermal lattice Boltzmann method, Phys. Rev. E **89**, 043303 (2014).

[15] B. Dorschner, N. Frapolli, S. S. Chikatamarla, and I. V. Karlin, Grid refinement for entropic lattice Boltzmann models, Phys. Rev. E **94**, 053311 (2016).

[16] P. Lallemand and L.-S. Luo, Hybrid finite-difference thermal lattice Boltzmann equation, Int. J. Mod. Phys. B **17**, 41 (2003).

[17] X. He and L.-S. Luo, Lattice Boltzmann model for the incompressible Navier-Stokes equation, J. Stat. Phys. **88**, 927 (1997).

[18] Z. Guo, C. Zheng, and B. Shi, Discrete lattice effects on the forcing term in the lattice Boltzmann method, Phys. Rev. E **65**, 046308 (2002).

[19] O. Malaspinas and P. Sagaut, Wall model for large-eddy simulation based on the lattice Boltzmann method, J. Comput. Phys. **275**, 25 (2014).

[20] T.-M. Liou and C.-S. Wang, Large eddy simulation of rotating turbulent flows and heat transfer by the lattice Boltzmann method, Phys. Fluids **30**, 015106 (2018).

[21] Q. Zou and X. He, On pressure and velocity boundary conditions for the lattice Boltzmann BGK model, Phys. Fluids **9**, 1591 (1997).

[22] T. Fusegi, J. Hyun, K. Kuwahara, and B. Farouk, A numerical study of three-dimensional natural convection in a differentially heated cubical enclosure, Int J. Heat Mass Transfer **34**, 1543 (1991).

[23] Y. Peng, C. Shu, and Y. T Chew, A 3D incompressible thermal lattice Boltzmann model and its application to simulate natural convection in a cubic cavity, J. Comput. Phys. **193**, 260 (2004).

[24] P. Wang, Y. Zhang, and Z. Guo, Numerical study of three-dimensional natural convection in a cubical cavity at high Rayleigh numbers, Int J. Heat Mass Transfer **113**, 217 (2017).

[25] H. Kawamura, H. Abe, and Y. Matsuo, DNS of turbulent heat transfer in channel flow with respect to Reynolds and Prandtl number effects, Int. J. Heat Fluid Flow **20**, 196 (1999).